

Long-distance transport of magnon spin information in a magnetic insulator at room temperature

L. J. Cornelissen^{1*}, J. Liu¹, R. A. Duine², J. Ben Youssef³ and B. J. van Wees¹

The transport of spin information has been studied in various materials, such as metals¹, semiconductors² and graphene³. In these materials, spin is transported by the diffusion of conduction electrons⁴. Here we study the diffusion and relaxation of spin in a magnetic insulator, where the large bandgap prohibits the motion of electrons. Spin can still be transported, however, through the diffusion of non-equilibrium magnons, the quanta of spin-wave excitations in magnetically ordered materials. Here we show experimentally that these magnons can be excited and detected fully electrically^{5–7} in a linear response, and can transport spin angular momentum through the magnetic insulator yttrium iron garnet (YIG) over distances as large as 40 μm . We identify two transport regimes: the diffusion-limited regime for distances shorter than the magnon spin diffusion length, and the relaxation-limited regime for larger distances. With a model similar to the diffusion-relaxation model for electron spin transport in (semi)conducting materials, we extract the magnon spin diffusion length $\lambda = 9.4 \pm 0.6 \mu\text{m}$ in a thin 200 nm YIG film at room temperature.

Recently, a great deal of attention is devoted to the investigation of thermally excited magnons, particularly in studies of the spin Seebeck effect in YIG (refs 8–12), for which the relaxation length of magnons was investigated in a local longitudinal spin Seebeck geometry¹³. Long-distance transport of thermally excited magnons was demonstrated very recently at $T = 23 \text{ K}$, using a non-local geometry¹⁴. However, thermal excitation is a nonlinear and relatively slow process and does not allow high-fidelity transport and conversion of information. To facilitate magnonic devices operating with a linear response at room temperature, the ideal signal pathway would be: input electronic charge signal \rightarrow electron spins \rightarrow magnons \rightarrow electron spins \rightarrow output charge signal. Information processing and transport can then be done in the magnon part of the pathway¹⁵.

Kajiwara *et al.*¹⁶ reported long-distance transmission of signals in YIG by spin-wave interconversion. However, in their experiment spin waves are excited by exerting a spin transfer torque^{17,18} (STT) on the magnetization large enough to overcome the intrinsic and interfacial Gilbert damping, driving the sample into ferromagnetic resonance (FMR). The STT was generated by the spin Hall effect (SHE) in a platinum layer, deposited on the YIG. Spin waves generated in this type of experiment typically have frequencies $f < 10 \text{ GHz}$ (refs 16,19,20), much smaller than the thermal energy ($hf \gg k_B T$), and are hence in the classical regime. Excitation of this

type of spin waves by the STT is a highly nonlinear process, where a threshold current density has to be overcome to compensate the damping of the specific spin-wave modes. Their experiments proved difficult to reproduce, but recently Collet *et al.* have shown that YIG nanostructures can be driven into FMR through the STT (ref. 21). Chumak *et al.*²² demonstrated long-range low-frequency spin-wave spin transport using radiofrequency magnetic fields to excite spin waves, which were detected by making use of the inverse spin Hall effect (ISHE) in platinum.

Here, we demonstrate for the first time the excitation and detection of high-frequency magnons (that is, quantized spin waves with $hf \approx k_B T$) through a spin accumulation in a paramagnetic normal metal layer, and their long-distance transport in YIG. Because the spin accumulation can be induced (through the SHE) and detected (through the ISHE) electrically, this method allows full electrical excitation and detection of magnon spin signals in the linear regime and provides a new route towards the development of low-power electronic devices, using magnons rather than electrons for the transport and processing of information.

We study the transport of magnons in a non-local geometry, shown schematically in Fig. 1a. The devices consist of platinum (Pt) strips, deposited on a thin YIG film (see Methods for fabrication details). One Pt strip functions as injector, another as detector (Fig. 1c). When a charge current I is sent through the injector, the SHE generates a transverse spin current. A spin accumulation μ_s then builds up at the Pt|YIG interface, pointing in the film plane. When the spin orientation of μ_s is parallel (antiparallel) to the average magnetization M , magnons are annihilated (excited), resulting in a non-equilibrium magnon population n_m in the YIG (refs 5–7; shown schematically in Fig. 1a,b). The non-equilibrium magnons diffuse in the YIG, giving a magnon current j_m from injector to detector. At the detector, the reciprocal process occurs: magnons interact at the interface, flipping the spins of electrons and creating a spin imbalance in the platinum (Fig. 1b). Owing to the ISHE, the induced spin current is converted into charge current, which under open-circuit conditions generates a voltage V . The non-local resistance is then $R_{nl} = V/I$.

As only the component of μ_s collinear to M contributes to magnon injection/detection, we expect to see a dependence of R_{nl} on the angle α (Fig. 1c) between the sample and an in-plane external magnetic field B that orients M (see Methods). We perform non-local measurements as a function of α by rotating

¹Zernike Institute for Advanced Materials, Physics of Nanodevices, University of Groningen, 9747 AG Groningen, The Netherlands. ²Institute for Theoretical Physics and Center for Extreme Matter and Emergent Phenomena, University of Utrecht, 3512 JE Utrecht, The Netherlands. ³Université de Bretagne Occidentale, Laboratoire de Magnétisme de Bretagne CNRS, 6 Avenue Le Gorgeu, 29285 Brest, France. *e-mail: L.J.Cornelissen@rug.nl

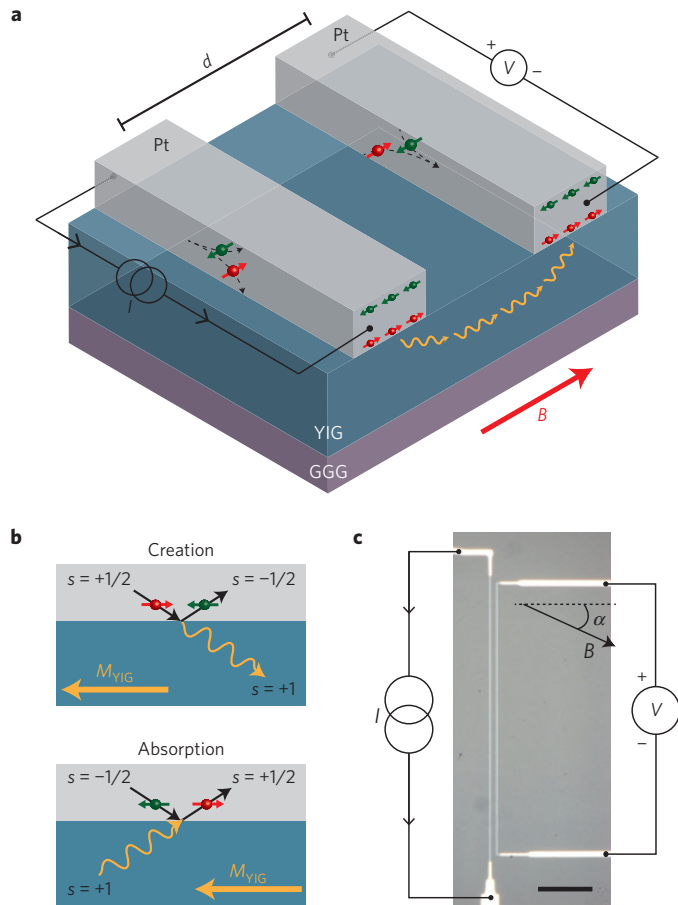


Figure 1 | Non-local measurement geometry. **a**, Schematic representation of the experimental geometry. A charge current I through the left platinum strip (the injector) generates a spin accumulation at the Pt|YIG interface through the spin Hall effect. Through the exchange interaction at the interface, angular momentum is transferred to the YIG, exciting or annihilating magnons. The magnons then diffuse towards the right platinum strip (the detector), where they are absorbed and a spin accumulation is generated. Through the inverse spin Hall effect the spin accumulation is converted to a charge voltage V , which is then measured. **b**, Schematic of the magnon creation and absorption process. A conduction electron in the platinum scattering off the Pt|YIG interface transfers spin angular momentum to the YIG. This will flip its spin and create a magnon. The reciprocal process occurs for magnon absorption. **c**, Optical microscope image of a typical device. The parallel vertical lines are the platinum injector and detector, which are contacted by gold leads. Current and voltage connections are indicated schematically. An external magnetic field B is applied at an angle α . The scale bar represents 20 μm .

the sample in a fixed external field. Using lock-in amplifiers, we separate higher-order contributions in the voltage by measuring higher harmonics, using: $V = R_1 I + R_2 I^2 + \dots$, where R_i is the i th harmonic response²³. Because magnon spin injection/detection scales linearly with I , its magnitude is obtained from the first harmonic signal. Any thermal effects due to Joule heating (for which $\Delta T \propto I^2$) will be detected in the second harmonic signal. The result of such a measurement is shown in Fig. 2a (2c) for the first (second) harmonic, and the observed angular dependence is explained schematically in Fig. 2b (2d).

We fabricated two series of devices with different injector–detector separation distances d . Series A is tailored to the short-distance regime ($d < 5 \mu\text{m}$), whereas series B explores the long-distance regime ($3 < d < 50 \mu\text{m}$). For each device, a non-local measurement as shown in Fig. 2 was performed.

The magnitudes of the non-local resistances were extracted for every d , by fitting the data with

$$R^{1\omega} = R_0^{1\omega} + R_{\text{nl}}^{1\omega} \cos^2(\alpha) \quad (1)$$

$$R^{2\omega} = R_0^{2\omega} + \frac{1}{2} R_{\text{nl}}^{2\omega} \cos(\alpha) \quad (2)$$

where $R_0^{1\omega}$ and $R_0^{2\omega}$ are offset resistances (see Methods) and $R_{\text{nl}}^{1\omega}$ ($R_{\text{nl}}^{2\omega}$) are the magnitudes of the first (second) harmonic signal. Figure 3a and c (3b and d) show the results on linear and logarithmic scales, for the first (second) harmonic non-local resistance, respectively. Both $R_{\text{nl}}^{1\omega}$ and $R_{\text{nl}}^{2\omega}$ are normalized to device length, to compare devices having different lengths.

From Fig. 3 we can clearly observe two regimes, which we interpret as follows: at large distances, signal decay is dominated by magnon relaxation and is characterized by exponential decay. For distances shorter than the magnon spin diffusion length we observe diffusive transport, and the signal follows a $1/d$ behaviour (inset Fig. 3a). Both regimes are described well with a single model, using the one-dimensional spin diffusion equation^{24,25}, adapted for magnon transport:

$$\frac{d^2 n_m}{dx^2} = \frac{n_m}{\lambda^2}, \quad \text{with } \lambda = \sqrt{D\tau} \quad (3)$$

where n_m is the non-equilibrium magnon density, λ is the magnon spin diffusion length in YIG, D is the magnon diffusion constant and τ is the magnon relaxation time. The one-dimensional approach is valid because the YIG thickness (200 nm) is much smaller than the injector–detector distance d , whereas the device length is much larger than d . We assume strong spin–magnon coupling between YIG and platinum, given the large spin-mixing conductance at the Pt|YIG interface^{26,27} and the strong spin–orbit interaction in platinum. We therefore impose the boundary conditions $n_m(0) = n_0$ and $n_m(d) = 0$, where n_0 is the injected magnon density, which is proportional to the applied current and is determined by various material and interface parameters. These conditions imply that the injector acts as a low-impedance magnon source, and all magnon current is absorbed when it arrives at the detector. The solution to equation (3) is of the form $n_m(x) = a \exp(-x/\lambda) + b \exp(x/\lambda)$, and from the boundary conditions we find for the magnon diffusion current density $j_m = -D(dn_m/dx)$ at the detector:

$$j_m(x=d) = -2D \frac{n_0}{\lambda} \frac{\exp(d/\lambda)}{1 - \exp(2d/\lambda)} \quad (4)$$

The non-local resistance is proportional to $j_m(d)/n_0$, and from equation (4) we adopt a two-parameter fitting function for the non-local resistances, capturing the distance-independent prefactors in a single parameter C :

$$R_{\text{nl}} = \frac{C}{\lambda} \frac{\exp(d/\lambda)}{1 - \exp(2d/\lambda)} \quad (5)$$

The signal decay described by equation (5) is equivalent to that of spin signals in metallic spin valves with transparent contacts²⁸. The dashed lines shown in Fig. 3a,c are best fits to this function, where we find from the first harmonic data $\lambda^{1\omega} = 9.4 \pm 0.6 \mu\text{m}$. From the second harmonic signal (Fig. 3b,d), originating from magnons generated by heat produced in the injector strip, we find $\lambda^{2\omega} = 8.7 \pm 0.8 \mu\text{m}$. For distances larger than 40 μm , the non-local voltage is smaller than the noise level of our set-up (approximately 3 nV_{r.m.s.}). We compare the magnitude and sign of the signal in the short-distance measurements to a local measurement in Supplementary Section A. From this, we obtain a value for the spin conductivity of YIG, $\sigma_s \approx 4 \times 10^5 \text{ S m}^{-1}$, which is comparable to that of metals.

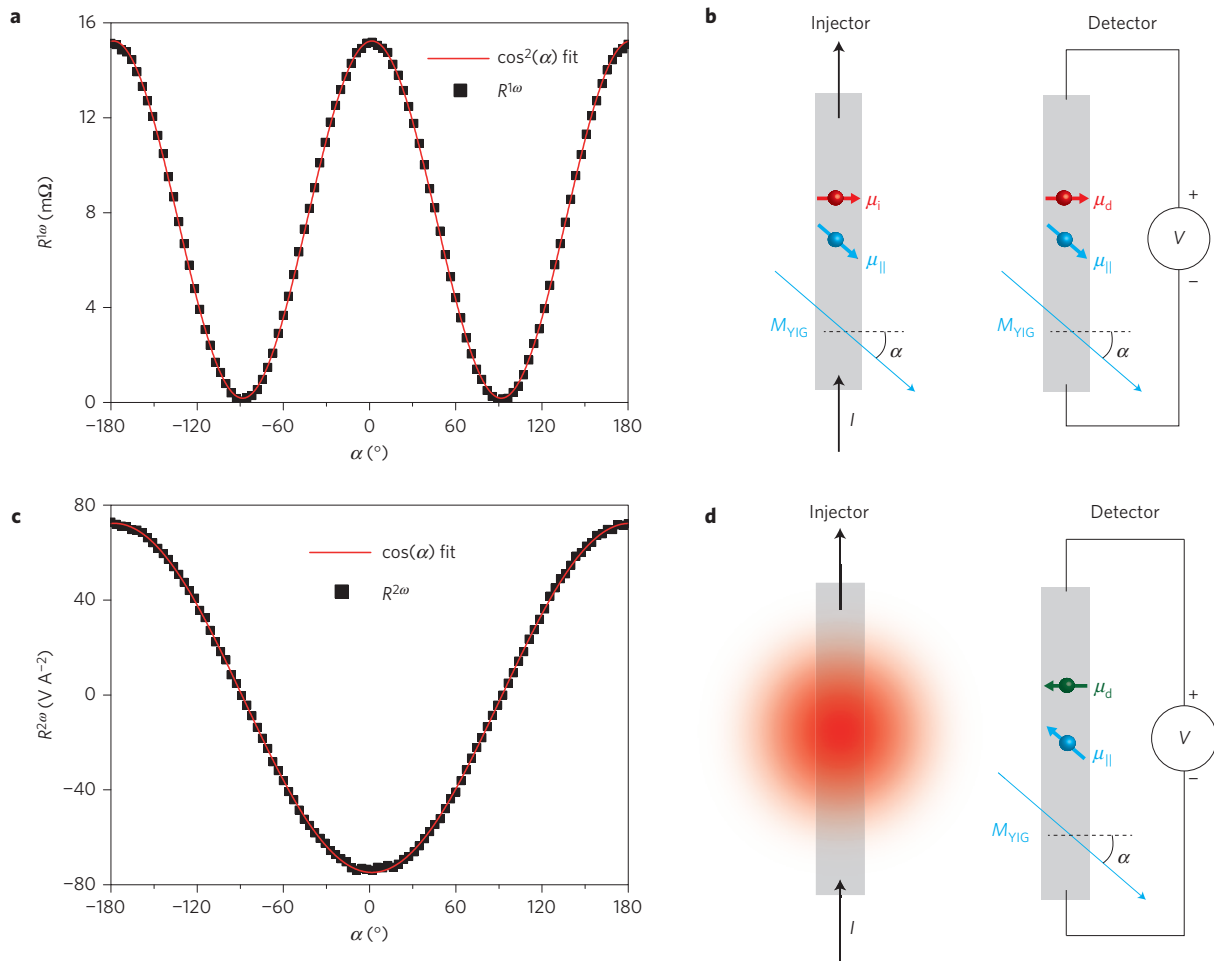


Figure 2 | Non-local resistance as a function of angle α . **a**, First harmonic signal. The red line is a $\cos^2\alpha$ fit through the data. **b**, Schematic top-view of the experiment. A charge current I through the injector generates a spin accumulation μ_i at the Pt/YIG interface. The component $\mu_{||}$ parallel to the net YIG magnetization M_{YIG} generates non-equilibrium magnons in the YIG, which gives rise to a $\cos\alpha$ dependence of the injected magnon density. The magnons then diffuse to the detector. At the detector, a spin accumulation $\mu_{||}$ parallel to M_{YIG} is generated. Owing to the inverse spin Hall effect, $\mu_{||}$ generates a charge voltage, of which we detect the component generated by μ_d . This gives rise to a $\cos\alpha$ dependence of the detected magnon current. The total signal is a product of the effects at the injector and detector, leading to the $\cos^2\alpha$ dependence shown in **a**. **c**, Second harmonic signal. The red line is a $\cos\alpha$ fit through the data. **d**, Schematic illustration of the angular dependence of the second harmonic: Joule heating at the injector excites magnons thermally, which diffuse to the detector. This process is independent of α . At the detector, the excited magnons generate a spin accumulation antiparallel to the YIG magnetization, which is detected in the same way as for the first harmonic, giving rise to a total $\cos\alpha$ dependence. The data shown in **a** and **c** are from a device with an injector–detector separation distance of 200 nm and a device length of 12.5 μm , measured at a lock-in frequency $f = 9$ Hz.

The first and second harmonic signals can be characterized by similar values of λ , indicating that thermally excited magnons are also generated in the close vicinity of the injector. This supports the conclusions drawn in ref. 14—namely, for thermal magnon excitation, the magnon signal reaches far beyond the thermal gradient generated by the applied heating. Note, however, that the sign change for the second harmonic signal (Fig. 3b inset) illustrates that the physics for electrical and thermal magnon generation is very different. This is discussed further in Supplementary Section B.

We verify our assumption of magnon excitation and detection in the linear regime by performing measurements where we reversed the role of injector and detector. The results are shown in Fig. 4a (4b) for the first (second) harmonic. For the first harmonic non-local resistance we find $R_{V-I}^{1\omega} = 13.28 \pm 0.02$ mΩ and $R_{I-V}^{1\omega} = 13.26 \pm 0.03$ mΩ. As we find $R_{V-I}(B) = R_{I-V}(-B)$ (ref. 29), we conclude that Onsager reciprocity holds within the experimental uncertainty, despite the asymmetry in the injector–detector geometry. Reciprocity does not hold for the second harmonic (Fig. 4b), as expected for nonlinear processes.

Finally, we verify that $V_{nl}^{1\omega}$ scales linearly with applied current (Fig. 4c). The linearity and reciprocity of the first harmonic non-local signal demonstrate that it is due to linear processes only.

Remarkably, the observed magnon transport is described well by the familiar spin diffusion model, despite the completely different character of the carriers of spins in magnetic insulators (bosons) compared to metals and semiconductors (fermions). Our results are consistent with spin injection/detection by invasive contacts, indicating that by optimizing contact properties the signals could be enhanced further. Our observation that the YIG spin conductivity is comparable to that of metals, combined with the long magnon spin diffusion length in YIG, provides new opportunities from a technological point of view to enable novel magnonic devices based on microstructured YIG. The observed similarity between electron and magnon transport begs the question how far this analogy can be extended, and calls for the investigation of effects such as the magnon Hall effect and, possibly, ballistic magnon transport at lower temperatures.

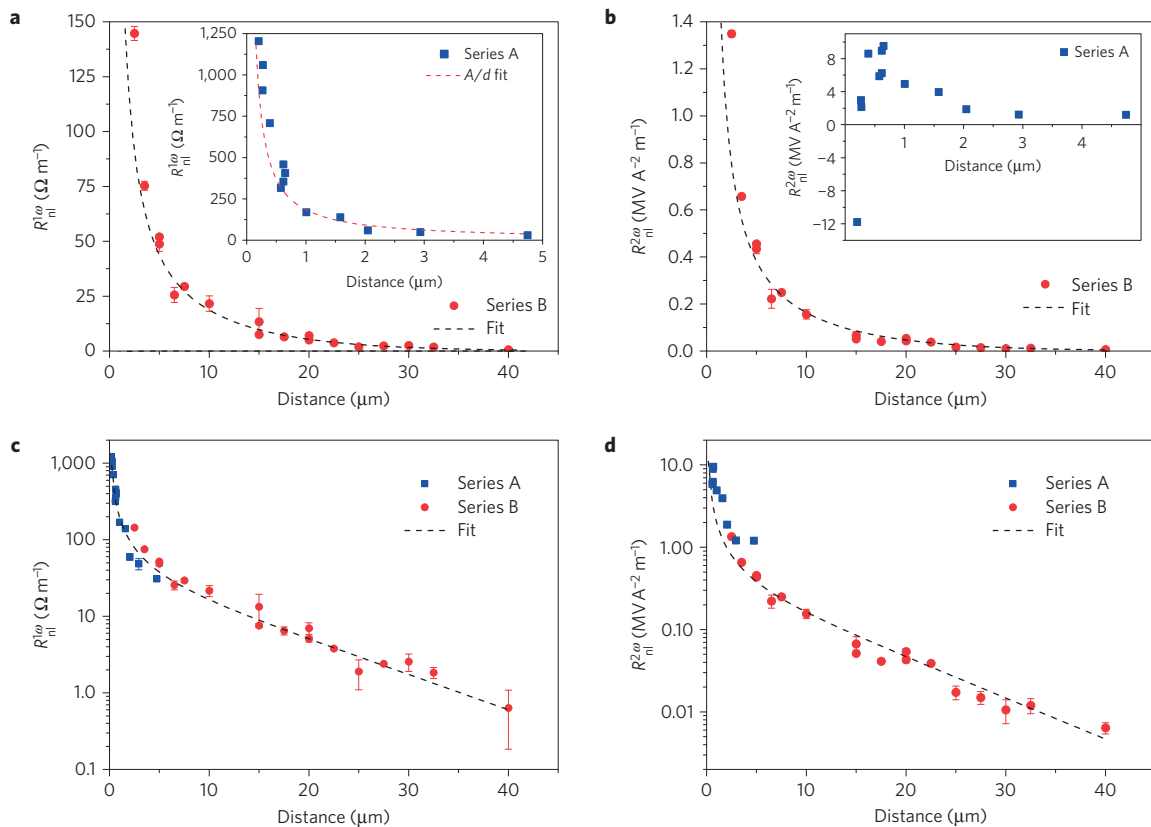


Figure 3 | Amplitude of the non-local signals as a function of injector-detector separation distance. Every data point represents a device with a different injector-detector separation and results from an angle-dependent measurement as shown in Fig. 2. The magnitude of the signal is extracted by fitting the angle-dependent non-local resistance to equation (1) (2) for the first (second) harmonic. The error bars represent the standard error in the fits. The signal is scaled by device length for both first and second harmonic. **a,c**, First harmonic data on linear and logarithmic scales, respectively. The dashed line is a fit to equation (1), resulting in $\lambda^{1\omega} = 9.4 \pm 0.6 \mu\text{m}$. For $d < \lambda$, the data is described well by a A/d fit, shown in the inset of **a**. **b,d**, Second harmonic data on linear and logarithmic scales, respectively. The dashed line is again a fit to equation (5), and we find $\lambda^{2\omega} = 8.7 \pm 0.8 \mu\text{m}$. The inset to **b** shows the short-distance behaviour of the second harmonic signal. For very short distances, the signal changes sign. For this reason, data points with $d < 0.5 \mu\text{m}$ were omitted from the fit in **b** and **d**.

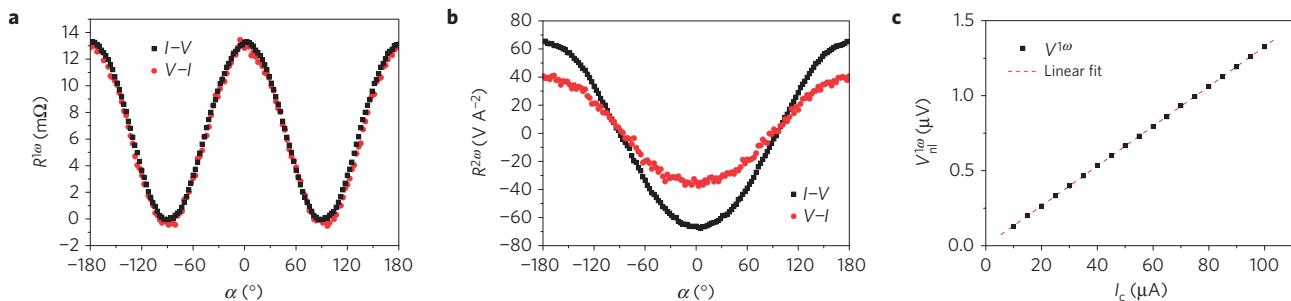


Figure 4 | Demonstration of reciprocity and linearity of the non-local resistance. **a**, First harmonic signal as a function of angle for the I - V and V - I configurations. We extract the amplitude of the signal using a fit to equation (1), finding $R_{V-I}^{1\omega} = 13.28 \pm 0.024 \text{ m}\Omega$ and $R_{I-V}^{1\omega} = 13.26 \pm 0.033 \text{ m}\Omega$. We thus conclude that reciprocity holds. **b**, Second harmonic signal as a function of angle. We extract the amplitude of the signal using a fit to equation (2), finding $R_{V-I}^{2\omega} = 76.3 \pm 0.5 \text{ V A}^{-2}$ and $R_{I-V}^{2\omega} = 132.8 \pm 0.5 \text{ V A}^{-2}$. We conclude that reciprocity does not hold for the second harmonic. **c**, Non-local voltage as a function of injected charge current. The data is obtained from angle-dependent measurements. A data point represents the amplitude of the angle-dependent voltage, obtained by a fit to equation (1). The error bars, representing the standard error in the fit, are also plotted but are smaller than the data points. The red dashed line is a linear fit through the data, showing the linearity of the first harmonic signal. The data shown here is obtained from a device with an injector-detector separation distance of 200 nm and a device length of 12.5 μm , measured at a lock-in frequency $f = 5.939 \text{ Hz}$.

Methods

Methods and any associated references are available in the [online version of the paper](#).

Received 22 May 2015; accepted 5 August 2015;
published online 14 September 2015

References

- Johnson, M. & Silsbee, R. H. Interfacial charge-spin coupling: Injection and detection of spin magnetization in metals. *Phys. Rev. Lett.* **55**, 1790–1793 (1985).
- Lou, X. *et al.* Electrical detection of spin transport in lateral ferromagnet-semiconductor devices. *Nature Phys.* **3**, 197–202 (2007).

3. Tombros, N., Jozsa, C., Popinciuc, M., Jonkman, H. T. & van Wees, B. J. Electronic spin transport and spin precession in single graphene layers at room temperature. *Nature* **448**, 571–574 (2007).
4. Fabian, J., Matos-Abiad, A., Ertler, C., Stano, P. & Zutic, I. Semiconductor spintronics. *Acta Phys. Slovaca* **57**, 565 (2007).
5. Zhang, S. S.-L. & Zhang, S. Magnon mediated electric current drag across a ferromagnetic insulator layer. *Phys. Rev. Lett.* **109**, 096603 (2012).
6. Zhang, S. S.-L. & Zhang, S. Spin convertance at magnetic interfaces. *Phys. Rev. B* **86**, 214424 (2012).
7. Bender, S. A., Duine, R. A. & Tserkovnyak, Y. Electronic pumping of quasiequilibrium Bose–Einstein-condensed magnons. *Phys. Rev. Lett.* **108**, 246601 (2012).
8. Uchida, K. *et al.* Spin Seebeck insulator. *Nature Mater.* **9**, 894–897 (2010).
9. Kikkawa, T. *et al.* Critical suppression of spin Seebeck effect by magnetic fields. *Phys. Rev. B* **92**, 064413 (2015).
10. Jin, H., Boona, S. R., Yang, Z., Myers, R. C. & Heremans, J. P. The effect of the magnon dispersion on the longitudinal spin Seebeck effect in yttrium iron garnets (YIG). Preprint at <http://arXiv.org/abs/1504.00895> (2015).
11. Schreier, M. *et al.* Magnon, phonon, and electron temperature profiles and the spin Seebeck effect in magnetic insulator/normal metal hybrid structures. *Phys. Rev. B* **88**, 094410 (2013).
12. Schreier, M. *et al.* Current heating induced spin Seebeck effect. *Appl. Phys. Lett.* **103**, 242404 (2013).
13. Kehlberger, A. *et al.* Determination of the origin of the spin Seebeck effect-bulk vs. interface effects. Preprint at <http://arXiv.org/abs/1306.0784> (2013).
14. Giles, B. L., Yang, Z., Jamison, J. & Myers, R. C. Long range pure magnon spin diffusion observed in a non-local spin-Seebeck geometry. Preprint at <http://arXiv.org/abs/1504.02808> (2015).
15. Chumak, A. V., Vasyuchka, V. I., Serga, A. A. & Hillebrands, B. Magnon spintronics. *Nature Phys.* **11**, 453–461 (2015).
16. Kajiwar, Y. *et al.* Transmission of electrical signals by spin-wave interconversion in a magnetic insulator. *Nature* **464**, 262–266 (2010).
17. Slonczewski, J. C. Current-driven excitation of magnetic multilayers. *J. Magn. Mater.* **159**, L1–L7 (1996).
18. Brataas, A., Bauer, G. E. W. & Kelly, P. Non-collinear magnetoelectronics. *Phys. Rep.* **427**, 157–255 (2006).
19. Gurevich, A. & Melkov, G. *Magnetization Oscillations and Waves* (CRC Press, 1996).
20. Serga, A. A., Chumak, A. V. & Hillebrands, B. YIG magnonics. *J. Phys. D* **43**, 264002 (2010).
21. Collet, M. *et al.* Generation of coherent spin-wave modes in Yttrium Iron Garnet microdiscs by spin-orbit torque. Preprint at <http://arxiv.org/abs/1504.01512> (2015).
22. Chumak, A. V. *et al.* Direct detection of magnon spin transport by the inverse spin Hall effect. *Appl. Phys. Lett.* **100**, 082405 (2012).
23. Bakker, F. L., Slachter, A., Adam, J.-P. & van Wees, B. J. Interplay of Peltier and Seebeck effects in nanoscale nonlocal spin valves. *Phys. Rev. Lett.* **105**, 136601 (2010).
24. Valet, T. & Fert, A. Theory of the perpendicular magnetoresistance in magnetic multilayers. *Phys. Rev. B* **48**, 7099–7113 (1993).
25. D'yakonov, M. I. & Perel, V. I. Possibility of orienting electron spins with current. *Sov. Phys. JETP Lett.* **13**, 467–469 (1971).
26. Jungfleisch, M. B., Lauer, V., Neb, R., Chumak, A. V. & Hillebrands, B. Improvement of the yttrium iron garnet/platinum interface for spin pumping-based applications. *Appl. Phys. Lett.* **103**, 022411 (2013).
27. Vlietstra, N., Shan, J., Castel, V., van Wees, B. J. & Ben Youssef, J. Spin-Hall magnetoresistance in platinum on yttrium iron garnet: Dependence on platinum thickness and in-plane/out-of-plane magnetization. *Phys. Rev. B* **87**, 184421 (2013).
28. Takahashi, S. & Maekawa, S. Spin injection and detection in magnetic nanostructures. *Phys. Rev. B* **67**, 052409 (2003).
29. Onsager, L. Reciprocal relations in irreversible processes. II. *Phys. Rev.* **38**, 2265 (1931).

Acknowledgements

We would like to acknowledge H. M. de Roos and J. G. Holstein for technical assistance, and would like to thank G. E. W. Bauer for discussions. This work is part of the research programme of the Foundation for Fundamental Research on Matter (FOM) and supported by NanoLab NL, EU FP7 ICT Grant No. 612759 InSpin and the Zernike Institute for Advanced Materials.

Author contributions

B.J.v.W. and L.J.C. conceived the experiments. L.J.C. designed and carried out the experiments, with help from J.L. J.B.Y. supplied the YIG samples used in the fabrication of sample series A. L.J.C., J.L., R.A.D. and B.J.v.W. were involved in the analysis. L.J.C. wrote the paper, with the help of the co-authors.

Additional information

Supplementary information is available in the [online version of the paper](#). Reprints and permissions information is available online at www.nature.com/reprints. Correspondence and requests for materials should be addressed to L.J.C.

Competing financial interests

The authors declare no competing financial interests.

Methods

Fabrication. The YIG samples of series A consist of a 200 nm (111) single-crystal YIG film grown on a 500 μm (111) $\text{Gd}_3\text{Ga}_5\text{O}_{12}$ (GGG) substrate by liquid-phase epitaxy (LPE), provided by the Université de Bretagne Occidentale in Brest, France. YIG samples of series B were obtained commercially from the company Matesy GmbH, and consist of a 210 nm single-crystal (111) $\text{Y}_3\text{Fe}_5\text{O}_{12}$ film grown by LPE, also on a GGG substrate. The saturation magnetization M_s and Gilbert damping parameter α are comparable for the YIG samples of series A and B, with $M_s^A \sim 140 \text{ kA m}^{-1}$, $\alpha^A \sim 2 \times 10^{-4}$ and $M_s^B \sim 144 \text{ kA m}^{-1}$, $\alpha^B \sim 1.4 \times 10^{-4}$. Values of M_s were obtained from superconducting quantum interference device (SQUID) magnetometry measurements, whereas the value for α was determined by means of FMR linewidth measurements (data obtained from N. Vlietstra and J.B.Y. for series A, and from Matesy GmbH for series B). The device pattern was defined using three e-beam lithography steps, each followed by a standard deposition and lift-off procedure. The first step produces a Ti/Au marker pattern, used to align the subsequent steps. The second step defines the platinum injector and detector strips, which were deposited by d.c. sputtering in an Ar^+ plasma at an argon pressure of 3.3×10^{-3} mbar. The deposited Pt thickness was approximately 13 nm for series A devices and 7 nm for series B devices, measured by atomic force microscopy. The third step defines 5/75 nm Ti/Au leads and bonding pads, deposited by e-beam evaporation. Before Ti evaporation, argon ion milling was used to remove any polymer residues from the platinum strips, ensuring electrical contact between the

platinum and the leads. Devices of series A have an injector/detector length of $L_A = 7.5$ to $12.5 \mu\text{m}$ and a strip width W_A of approximately 100–150 nm. Devices of series B have an injector/detector length of $L_B = 100 \mu\text{m}$ and a strip width W_B of approximately 300 nm.

Measurements. All measurements were carried out by means of three SR830 lock-in amplifiers using excitation frequencies ranging from 3 to 40 Hz. The lock-in amplifiers are set up to measure the first, second and third harmonic responses of the sample. Current was sent to the sample using a custom built current source, galvanically isolated from the rest of the measurement equipment. Voltage measurements were made using a custom-built pre-amplifier (gain 10^3 – 10^5) and amplified further using the lock-in systems. The current applied to the sample ranged from 10 to 200 μA (root mean squared). The typical excitation current used is $I = 80 \mu\text{A}$, which results in a charge current density of $j_c \approx 10^{10} \text{ A m}^{-2}$, depending on the specific device geometry. The in-plane coercive field of the YIG is $B_c < 1 \text{ mT}$ for both YIG samples, and we apply an external field to orient the magnetization (typically $B_{\text{ext}} = 5 \text{ mT}$) using a GMW electromagnet. The sample was rotated with respect to the magnet poles using a rotatable sample holder with stepper motor. The offset resistances $R_0^{1\omega}$ and $R_0^{2\omega}$ described in equations (1) and (2) depend on the capacitive and inductive coupling between the measurement wires to and from the sample, and vanish for low excitation frequencies (typically when $F_{\text{lock-in}} < 5 \text{ Hz}$).